Supplementary Materials for

Highly Stable Preferential CO Oxidation by Dinuclear Heterogeneous Catalysts

Yanyan Zhao[1#], Sheng Dai[2#], Ke R. Yang[3#], Sufeng Cao[1,4], Kelly L. Materna[3], Hannah M. C. Lant[3], Li Cheng Kao[5], Xuefei Feng[5], Jinghua Guo[5], Gary W. Brudvig[3], Maria Flytzani-Stephanopoulos[4], Victor S. Batista[3]*, Xiaoqing Pan[2]*, Dunwei Wang[1]*

1. Department of Chemistry, Merkert Chemistry Center, Boston College, 2609 Beacon Street, Chestnut Hill, Massachusetts 02467, USA
2. Department of Physics and Astronomy, University of California–Irvine, Irvine, California 92697, USA
3. Yale Energy Sciences Institute and Department of Chemistry, Yale University, New Haven, Connecticut 06520, USA
4. Department of Chemical and Biological Engineering, Tufts University, 4 Colby Street, Medford, Massachusetts 02155, USA
5. Advanced Light Source, Lawrence Berkeley National Laboratory, Berkeley, California 94720, USA

# These authors contributed equally to this work.

* Correspondence to: victor.batista@yale.edu; xiaoqinp@uci.edu; and dunwei.wang@bc.edu

Experimental details:

Catalyst Preparation

Preparation of Ir catalyst on CeO_2 and loading estimation

Nanoparticle CeO_2 was purchased from US Research Nanomaterials, Inc with a surface area of 35-70 m^2/g and was used as the support for various Ir/CeO_2 catalysts. Prior to catalyst preparation, the support was calcined in air at 400 °C for 4 h, then stored under a vacuum in the dark.

The preparation of the Ir homogenous dimer solution was based on previously established methods (*1*). The monomer for the dimer solution preparation, Cp*Ir[pyalc(OH)] (Cp*: pentamethylcyclopentadienyl, $C_5Me_5^-$, pyalc: 2-(2-pyridyl)-2-propanolate), was synthesized following an established procedure [1, 2]. The CeO_2 substrate as treated above was soaked and stirred in 5 M Ir homogenous dimer solution for 30 h. The samples were obtained by filtering, washing with DI water at 50 °C, and then drying in the vacuum oven. The procedure was repeated 3 times. Afterwards, it was further treated by photochemical methods using a UVO cleaner system (Jelight Company Inc.) for 50 min to remove organic ligands. The obtained catalysts were calcined in 10% H_2 (bal. He) at 130 °C for 2 h to yield Ir DHC/CeO_2. Ir SAC was prepared by a similar procedure but with 70 min UV treatment and 2.5 h calcination. Inductively coupled plasma (ICP) spectroscopy confirmed the Ir loading as ca. 1 wt.%. The as-prepared catalysts were stored under a vacuum in the dark for all characterizations.

Preferential CO oxidation activity tests

Preferential CO oxidation (CO PROX) reactions were performed in a continuous flow reactor at ambient pressure. The reactant gases (1% CO, 1% O_2, 40% H_2, bal. He, purchased from Airgas) were introduced into the reaction system by a mass flow controller connected to the cylinder. The catalyst bed was composed of the solid powder of supported catalysts and inert quartz. The ramping rate of temperature was set at 5 °C/min. The mixed gases passing through the catalysts bed were analyzed by an online mass spectrometer. The conversion of CO was calculated by equation **I**. CO conversion was controlled between 8-20% to permit steady-state kinetic study. Each sample was pelleted into particles (50-125 μm) and placed on the glass wool in the cell and then pretreated by 10% H_2 (bal. He) at 130 °C for 1 h.

$$CO\ conversion = \frac{CO_{in} - CO_{out}}{CO_{in}} \qquad \text{(I)}$$

CO diffuse reflectance infrared Fourier transform spectroscopy

CO diffuse reflectance infrared Fourier transform spectroscopy (CO-DRIFTS) was done by using a Nicolet iS50 FTIR spectrometer equipped with a mercury cadmium telluride detector and a Harrick praying mantis HVC-DRP4 cell with KBr windows. Each sample was pelleted into particles (50-125 μm) and placed on the glass wool in the cell and then pretreated by pure He at 105 ^{o}C for 1 h. The background spectra were collected at RT. The spectra were collected with a resolution of 4 cm^{-1} and 128 scans. The catalyst powder was purged with diluted CO for 30 min and then pure He to desorb physically adsorbed CO, at which time the data were collected.

X-ray absorption spectroscopy

The *in-situ* X-ray absorption spectroscopy (XAS) data were collected in fluorescence mode with a 13-channel germanium detector. The facility is located at the Advanced Photon Source (APS) at Argonne National Lab. The Ir L_3 absorption edge energy was calibrated by measurement on an Ir foil with energy of 11215 eV. Sixteen consecutive scans were collected for each data point. For the *in-situ* XAS experiments, the samples were pretreated under the reaction condition (20 mL/min flow rate, 1% CO, 1% O_2, 40% H_2, bal. He, 473 K, ~10 mg catalyst loading) for 2 h and then the data were collected after the temperature was decreased to room temperature (with reactant gases flowing).

The *ex-situ* Ir L_3-edge XAS data were collected at the Advanced Light Source (ALS) at Lawrence Berkeley National Laboratory, bending magnet microprobe beamline 10.3.2 (2.1- 17 keV) with the storage ring operating at 500 mA and 1.9 GeV, using a Si (111) double-crystal monochromator. All data were collected under ambient conditions in fluorescence mode at the Ir L_3-edge (11215 eV). The monochromator energy was calibrated using an Ir foil, with the 1st derivative maximum set to 11215 eV. Fluorescence emission counts were recorded with a seven-element Gesolid-state detector (Canberra) and XIA electronics. Ir L_3-edge X-ray absorption spectra were recorded in fluorescence mode from 11060 to 12200 eV, by continuously scanning the Si (111) monochromator (Quick XASmode). All data were processed using the LabVIEW custom beamline 10.3.2 software to perform deadtime correction, energy calibration, glitch removal, pre-edge subtraction, and post-edge normalization. EXAFS spectra were recorded up to

985 eV above the edge (i.e., up to k ≈ 12.5 $Å^{-1}$), and 20 scans were averaged. To be noted, the *ex-situ* EXAFS was tested without inert atmosphere protection and might induce oxidation state change of metal center, which will not undermine the key information.

Scanning transmission electron microscopy

Aberration-corrected scanning transmission electron microscopy (AC-STEM) was performed on a JEOL Grand ARM300CF microscope equipped with two spherical aberration correctors, operated at 200 kV. High angle annular dark field (HAADF)-STEM images were recorded using a convergence semi-angle of 22 mrad, and inner- and outer- collection angles of 83 and 165 mrad, respectively. The *in situ* STEM experiment was performed using a Denssolution Climate system, which allows for dynamic observation of materials heated under atmospheric pressure inside a transmission electron microscope.

Discussion on electron beam effect for *in-situ* STEM experiment under gas phase condition

In order to minimize effects of the electron beam during the *in-situ* STEM experiment under gas-phase conditions, a very small probe current (<10 pA) was used for *in-situ* STEM imaging. Typical probe currents for normal STEM imaging are between 50-100 pA. Meanwhile, the magnification was always kept below 8.0 M, and the acquisition time was controlled to be less than 12 seconds to reduce the electron dose. Considering the imaging condition (a pixel dwell time of 12 μs/pixel and a pixel size of 0.08 $Å^2$) of our STEM observation, the electron dose we used was less than 1.0×10^4 e/$Å^2$, which is about 2 orders of magnitude lower than typical values for atomic-resolution STEM imaging. Particularly, the electron beam was turned off except during image collection for the *in-situ* STEM experiment. According to the experimental evidence, the Ir DHC and the CeO_2 support were stable during the *in-situ* STEM experiment, and no obvious irradiation damage was found during image collection.

Moreover, additional experiments were carried out to compare images of the same area before and after exposure to the electron beam during image acquisition. Here, Fig. S11A is an image taken under an inert atmosphere (760 Torr of N_2) at 473 K, showing an Ir single atom on the CeO_2 support, as indicated by the yellow circle. Then, one more image was taken afterwards, using the same imaging condition, as shown in Fig. S11B. Apparently, no obvious motion of this Ir atom was observed according to the comparison between Figs. S11A and S11B, confirming that the beam condition we used did not introduce a movement of Ir atoms on the CeO_2 surface under the

gas phase condition. Therefore, these results rule out the possible artifact from the electron beam effect, and the observed Ir atom motion in our *in-situ* experiment was indeed caused by the pseudo-PROX reaction condition.

Computational details:

All periodic boundary calculations were performed with the Vienna Ab initio Simulation Package (VASP) [3-6]. We use the Perdew-Burke-Ernzerhof (PBE) [7] exchange-correlation functional in conjugation with the projected-augmented wave (PAW) method [8, 9]. A cutoff energy of 500 eV was chosen for the plane wave basis set in all calculations. We used the Gaussian smearing method to accelerate SCF convergence and the σ value was chosen to be 0.1 eV. Dispersion interactions were considered using Grimme's D3 empirical correction with Becke-Johnson damping [10]. The standard GGAs fail for strongly correlated systems such as the d electrons of Ir and f electron of Ce. All calculations involving Ir and Ce atoms were performed with the spin-polarized DFT+U method, using the rotational-invariant formalism developed by Dudarev *et al.* [11]. The empirical U_{eff} parameters were chosen to be 5.0 eV for Ce 4f orbitals [12, 13] and 3.0 eV for Ir 5d electrons [14].

A 5 × 5 × 5 Monckhorst-Pack type k-point grid [15] was chosen for the optimization of bulk ceria. The energy convergence criterion was set to be 10^{-6} eV per unit cell and the geometry convergence criterion was set to be 10^{-5} eV per unit cell for energy difference between two consecutive ionic steps. The optimized lattice constant is 5.46 Å, in good agreement with the experimental lattice constant of 5.41 Å [16].

We prepared slab models for the CeO_2 (110) surface to study Ir SAC and DHC since the CeO_2 (110) facet provides surface O atom pairs to bind Ir SAC and DHC. In addition, it is also the facet observed in our HAADF-STEM experiments. We constructed the atomic model of Ir DHC according to the following reasons. First of all, only OH_2, OH, and O are possible ligands for Ir under our experimental condition since organic ligands were removed after a long time of e UV-ozone treatment using a UVO cleaner system (Jelight Company Inc.) Secondly, surface O pairs on the surface provide binding sites for Ir atom in Ir DHC (Fig. S1), which provides two ligands per Ir. Thirdly, two Ir centers are connected by a mono-μ-oxo bridge to be consistent with an Ir–Ir distance of 3.7 Å suggested by HAADF-STEM and to be consistent with the homogeneous mono-μ-oxo bridged Ir dimer before anchoring onto the surface. The mono-μ-oxo bridge and two surface O atoms leave three open sites for each Ir center, which could be coordinated by OH_2, OH^-, or O^{2-}. Then, based on the oxidation state of Ir(IV), we found three OH^- could not only complete the

coordination sphere of Ir centers but also neutralize the charge. Therefore, we prepared the initial structures of Ir DHC with a mono-μ-oxo bridge, and three OH^- ligands, anchored by two surface O atoms on the CeO_2 surface. We then explored many Ir DHC structures with one μ-oxo bridge and three OH^- ligands, and the three most stable structures are shown in **Fig. S2**, and the most stable Ir DHC structure was used for the following mechanistic study. The atomic model of Ir SAC was constructed for the same reason to have four OH^- to neutralize the charge of Ir(IV) and to complete the coordination sphere of Ir along with two surface O atoms.

The lattice constants from the bulk optimization were fixed for all our slab calculations. We calculated the surface energy of the CeO_2 (110) facet with 4, 5, and 6 layers of Ce and O atoms and found that the calculated surface energy already converges with 4 layers of Ce and O atoms (Table S1). Therefore, we constructed slab models of the CeO_2 (110) facet with 4 layers of Ce and O atoms to study the stability and reactivity of Ir SAC and DHC. A vacuum layer of ~ 20 Å is used to minimize the artificial interactions between periodic images. A supercell of 15.44 Å × 30.44 Å × 10.92 Å was used to model the CeO_2 (110) surface, which contains 4 layers of Ce and O atoms (Figure S1). The atoms in the bottom two layers were fixed at their bulk position, while the atoms in the top two layers, as well as the adsorbates, were allowed to relax during geometry optimization. A 1 × 1 × 1 Monckhorst-Pack type k-point grid was used for all surface structure relaxations unless otherwise noted. The energy convergence criterion was set to be 10^{-5} eV per super cell and the force convergence criterion of 0.03 eV $Å^{-1}$. The nudged elastic band (NEB) method [17] was used to get the initial guess for transition states, which were fully optimized with the improved dimer method [18] implemented in VASP. The climbing image nudged elastic band (CI-NEB) method [17] was used to find the minimum-energy path (MEP) and get the initial guess for transition states. The force convergence criterion for CI-NEB calculation was set to be 0.10 eV $Å^{-1}$. Some transition states were fully optimized with the improved dimer method [18] implemented in VASP.

The calculations of isolated small molecules were performed with a supercell of 15.0 Å × 15.0 Å × 15.0 Å. The Gaussian smearing method and a σ value of 0.1 eV were used in the calculations. A 1 × 1 × 1 Monckhorst-Pack type k-point grid was used to sample the Brillouin zone and the SCF convergence criterion was set to be 10^{-5} eV per unit cell.

We have included all optimized structures for reproducibility at https://zenodo.org/ (DOI: 10.5281/zenodo.4771202).

EXAFS fitting:

The classical EXAFS equation is shown below

$$\chi(k) = \sum_{j}^{\text{paths}} N_j S_0^2 \frac{|f(k)|}{kR_j^2} \sin(2kR_j + 2\delta_c + \phi) e^{-2R_j/\lambda(k)} e^{-2\sigma^2 k^2}, \quad \text{(S1)}$$

where j goes over all scattering paths, k is the momentum vector, $2\delta_c + \phi$ is phase shift. The structural parameters are the interatomic distances R_j, the coordination number (or number of equivalent scatterers) N_j, and the temperature-dependent root-mean-square (rms) fluctuation in bond length σ, which also includes effects due to structural disorder. In addition, $f(k) = \left| f^{\text{eff}}(k) \right| e^{i\phi(k)}$ is the backscattering amplitude, δ_c is central-atom partial-wave phase shift of the final state, and $\lambda(k)$ is the energy-dependent XAFS mean free path. S_0^2 is the overall amplitude factor.

Isotropic Ir L_3-edge EXAF spectra of considered structures were calculated using the *ab initio* real space Green function approach as implemented in the FEFF program (version 6) [19]. The experimental EXAFS data $\chi(E)$, that is the fractional change in absorption coefficient of Ir atoms induced by neighboring atoms, are converted into momentum (k) space using the transformation $k = \left[\frac{2m_e}{(h/2\pi)^2} (E - E_0) \right]^{1/2}$, where m_e is the mass of the electron and h is the Planck's constant. The calculated EXAFS data are obtained by fitting the energy of the absorption edge (E_0) and the reduced factor (S_0^2) against the experimental results, using the IFEFFIT code [20].

All calculations using Feff6 were performed using the following parameters: "NLEG 8", and "CRITERIA 10.0 9.0", "RMAX 5.5", and "HOLE 4 1.0". A fractional cosine-square (Hanning) window with $\Delta k = 1$ was applied to the experimental and calculated EXAFS data. A grid of k points equally spaced at 0.05 Å^{-1} was used for the Fourier transformation (FT) of in the k range of 3.0-12.0 Å^{-1} for Ir DHC. The DFT optimized Ir DHC structures were used to calculate the scattering amplitude, phase shift, XAFS mean free path in Eq. (S1), while the edge shift ΔE_0 and the Debye-Waller factors (DWF) σ^2 were determined using IFEFFIT. The simulated EXAFS results are given in Figure S4 and the fitting and structural parameters in the EXAFS simulation are given in Table S2.

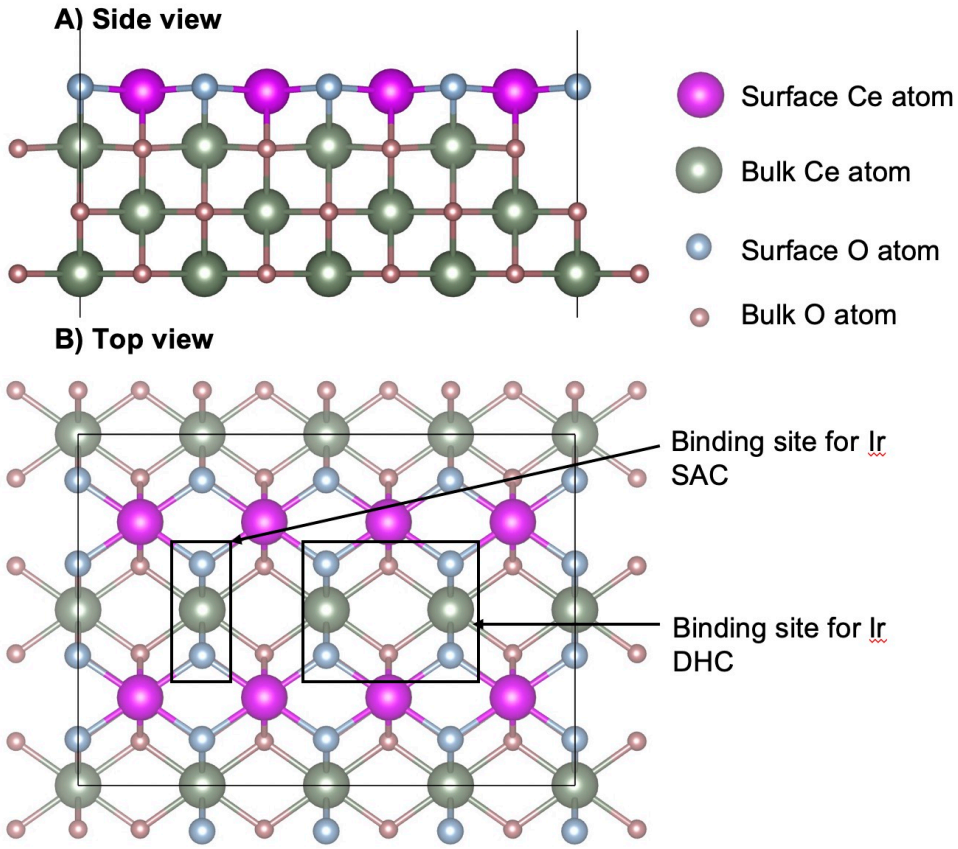

Figure S1. Side view **(A)** and top view **(B)** of the optimized CeO_2 (110) facet with surface O pairs as possible binding sites for Ir SAC and DHC. Once Ir DHC and SAC are anchored on the surface, the binding surface O is regarded as the interfacial O.

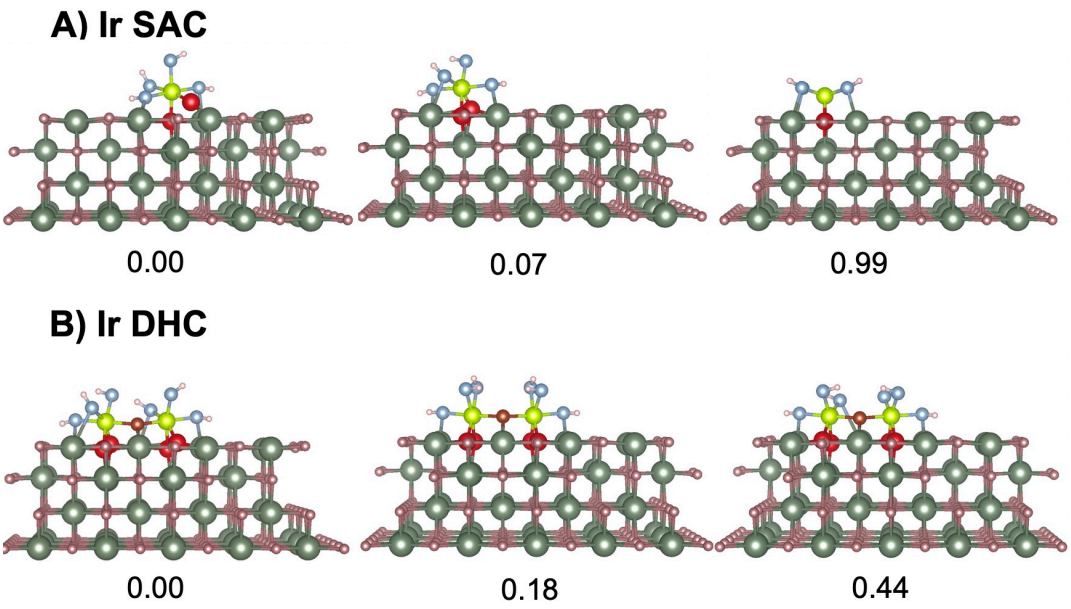

Figure S2. Low energy isomers of A) Ir SAC and B) DHC on CeO_2 (110) surface and their relative energies in the unit of eV. Ir SAC and DHC can be anchored on the CeO_2 (110) surface at the O pair binding sites indicated in Figure S1. The structural models of fresh Ir SAC and DHC are constructed by assigning Ir centers in oxidation state (IV) and adding water-derived ligands to balance the charge and coordinate to the Ir centers. We have explored many different structures of Ir SAC and DHC on CeO_2 (110) surface and the three most stable isomers for Ir SAC and Ir DHC are shown in Figure S2. We use yellow, green, and black spheres to represent Ir, Ce, and C atoms; blue, brown, red, and brandy rose balls represent O atoms in interfacial OH groups, bridge O atoms, interfacial O atoms, and O atoms in the CeO_2 bulk and other environments unless otherwise specified.

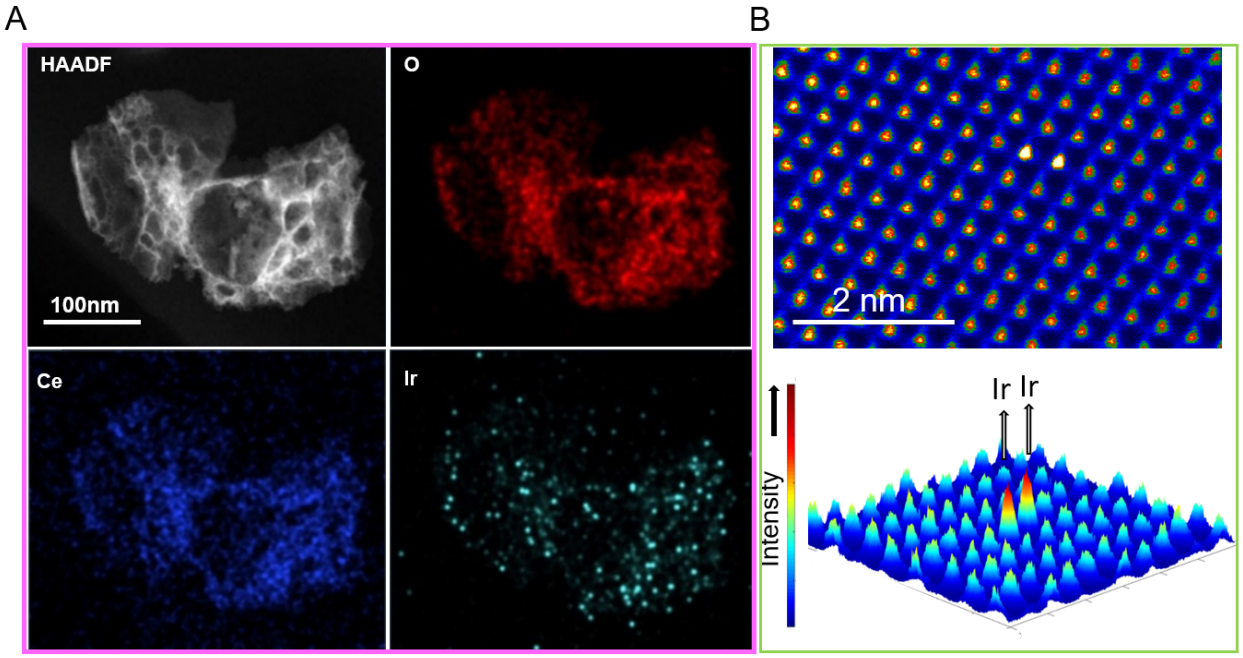

Figure S3. STEM characterization of Ir DHC on CeO_2. (**A**) HAADF-STEM images and EDS elemental mapping of Ce, O and Ir in the same region. (**B**) A false-colored magnified HAADF-STEM image of a single Ir DHC on CeO_2 and corresponding 3D intensity profile taken along the single Ir DHC.

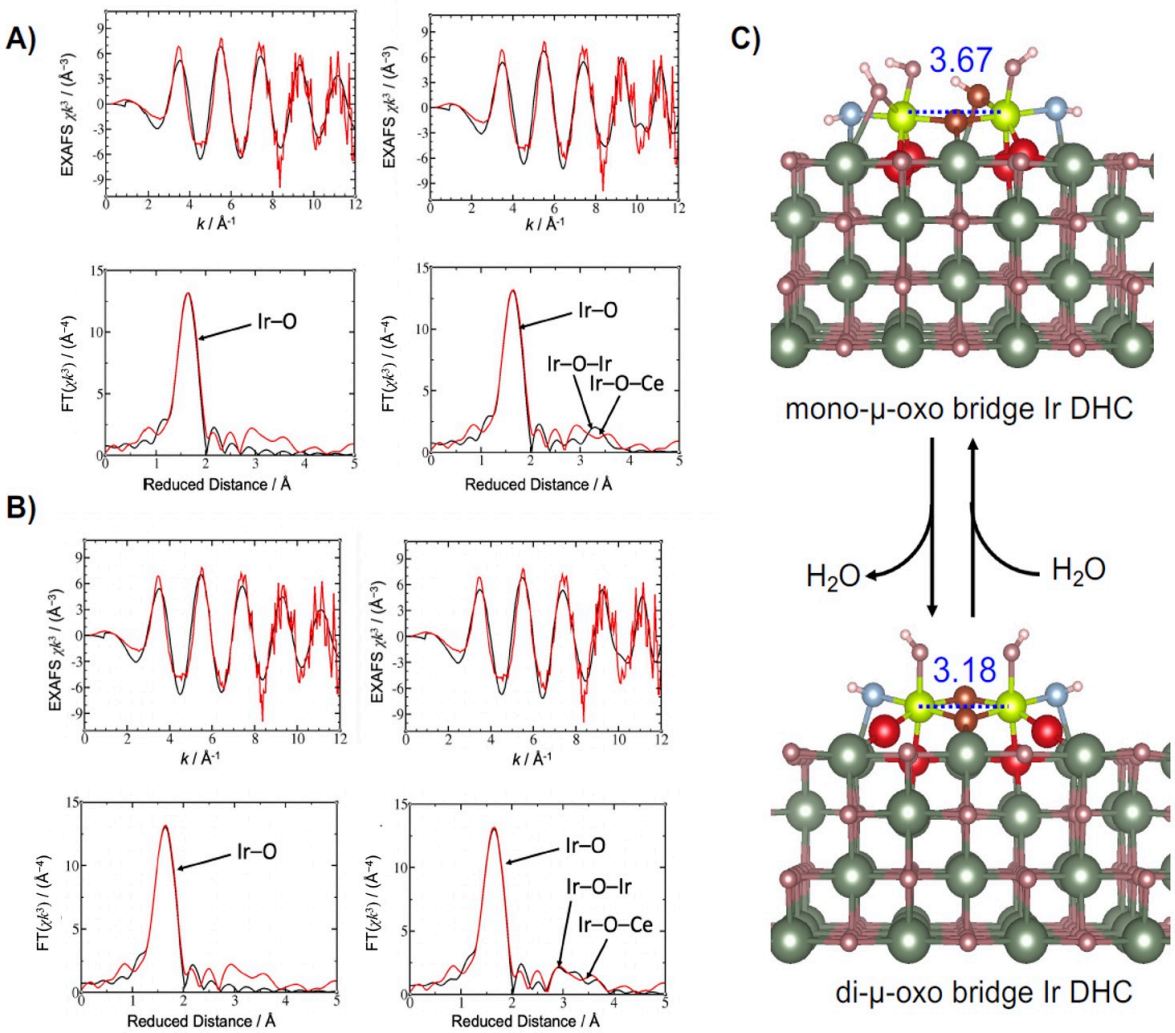

Figure S4. Experimental (Red) and calculated (black) EXAFS spectra of Ir DHC models in both *k* and reduced distance *R* space. A) Ir DHC connected by a mono-μ-oxo bridge; **B)** Ir DHC connected by a di-μ-oxo bridge; **C)** interconversion of mono-μ-oxo Ir DHC and bi-μ-oxo Ir DHC on the CeO_2 surface. The DFT optimized Ir DHC structures were used to calculate the EXAFS spectra. In left panels, only the first coordinate shell (Ir–O) was included in the EXAFS simulation, while in right panels, both the first coordination shell (Ir–O) and second coordination shell (Ir–O–Ir and Ir–O–Ce) were included. The comparison between the experimental and calculated EXAFS spectra suggests the Ir DHC probed by EXAFS is best described by a di-μ-oxo structure with a Ir–Ir distance of 3.2 Å. The mono-μ-oxo Ir DHC has an Ir–Ir distance too long to be consistent with EXAFS. However, the Ir–Ir distance in the mono-μ-oxo Ir DHC is consistent with the Ir–Ir distance (3.7 Å) obtained from the STEM measurements. Moreover, since the Ir DHC is prepared from a homogeneous Ir dimer connected by a mono-μ-oxo bridge, we anticipate the mono-μ-oxo bridge structure is the nature form of our Ir DHC on CeO_2 surfaces. As shown in **C)**, the mono-μ-oxo and di-μ-oxo Ir DHCs can interconvert by releasing or reacting with a water molecule. Our results indicate the dynamic change of Ir DHC on metal oxide surfaces happens under different characterization conditions and various techniques are needed to get more comprehensive pictures of catalysts on the support surface.

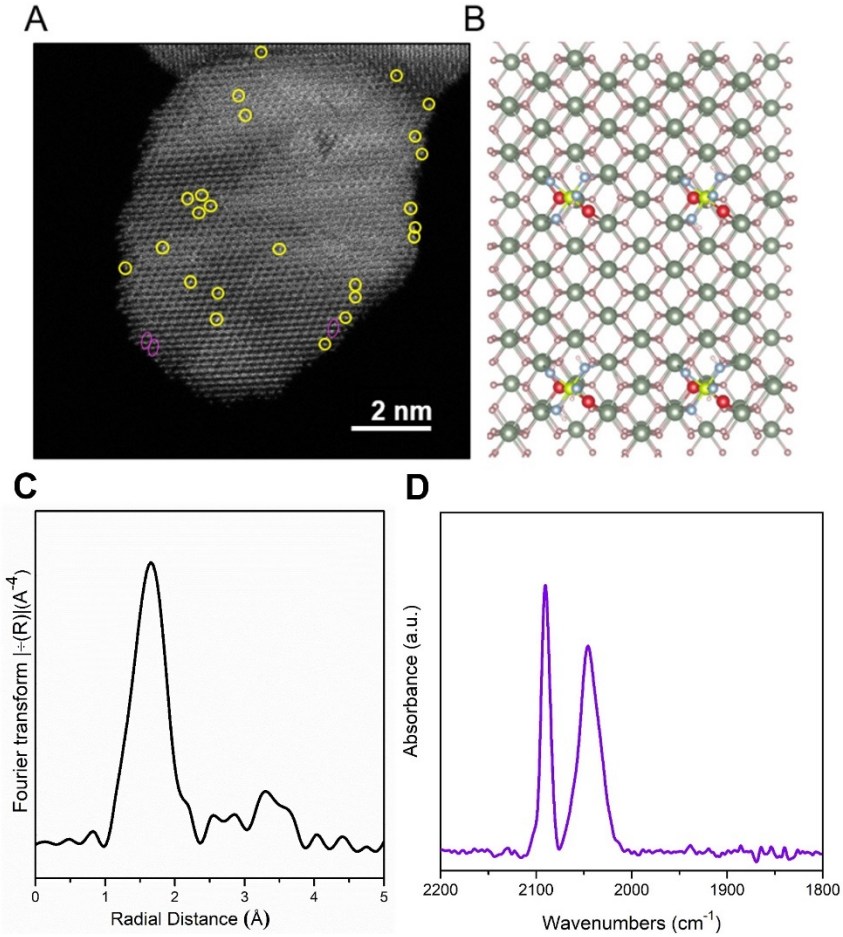

Figure S5. (**A**) HAADF-STEM characterization of Ir SAC on CeO_2. (**B**) DFT-optimized model of Ir SAC on CeO_2 (110) facet. EXAFS (**C**) and CO DRIFTS (**D**) characterization of Ir SAC.

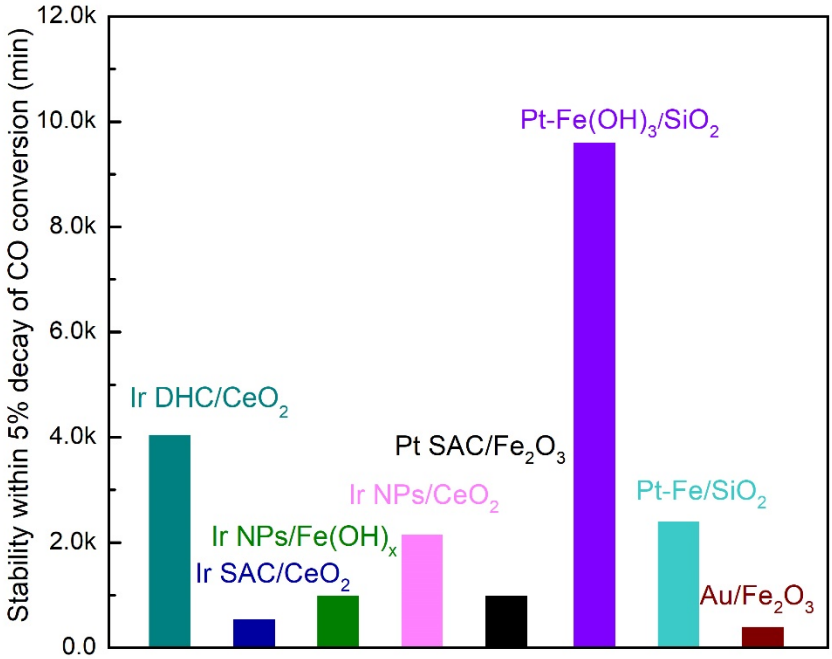

Figure S6. The stability comparison between Ir DHC and other catalysts reported in the literature (*21-25*).

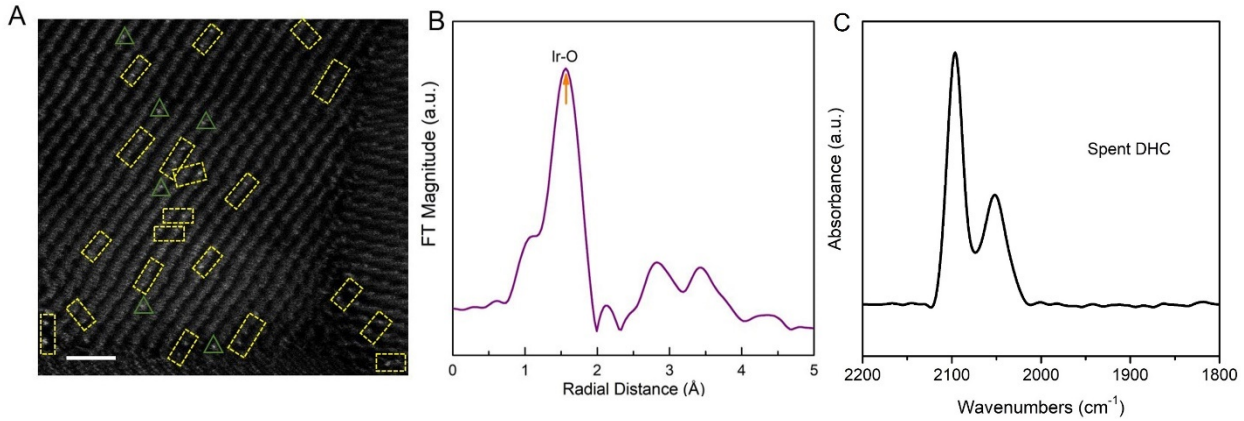

Figure S7. (**A**) HAADF-STEM (**B**) EXAFS and (**C**) CO DRIFTS characterization of Ir DHC after 180 h. Scale bar: 1 nm. The dual atomic pair was indicated by yellow rectangles and the single atom was indicated by green triangles.

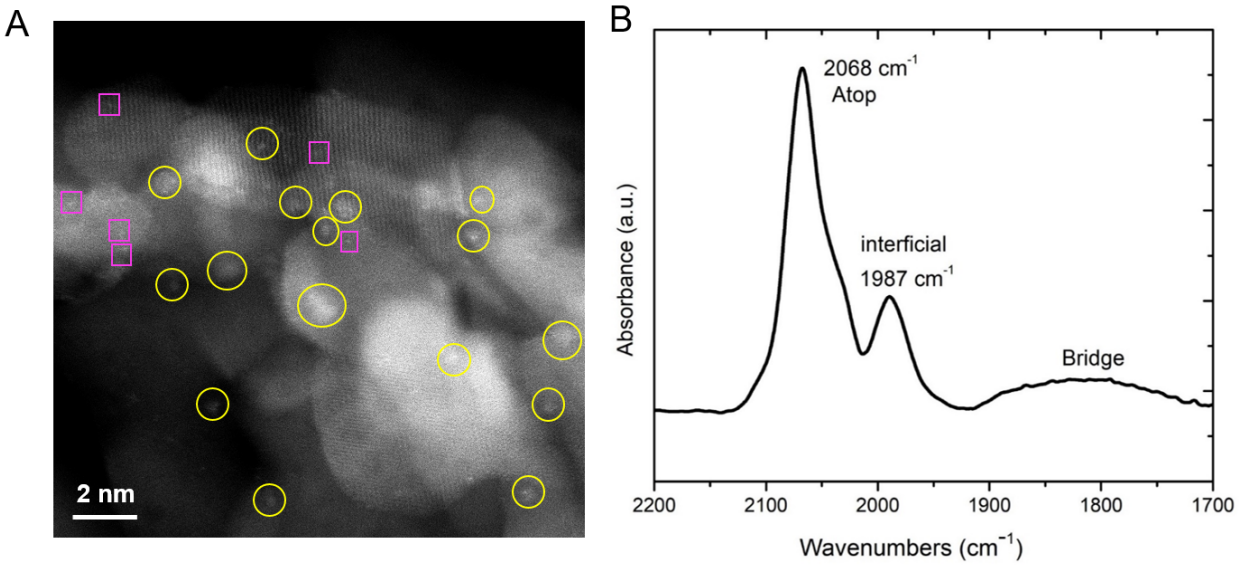

Figure S8. (**A**) HAADF-STEM and (**B**) *In-situ* DRIFTS spectra of Ir SAC after 180 h. Nanoclusters and nanoparticles were indicated by yellow circles and single atoms were indicated by pink circles.

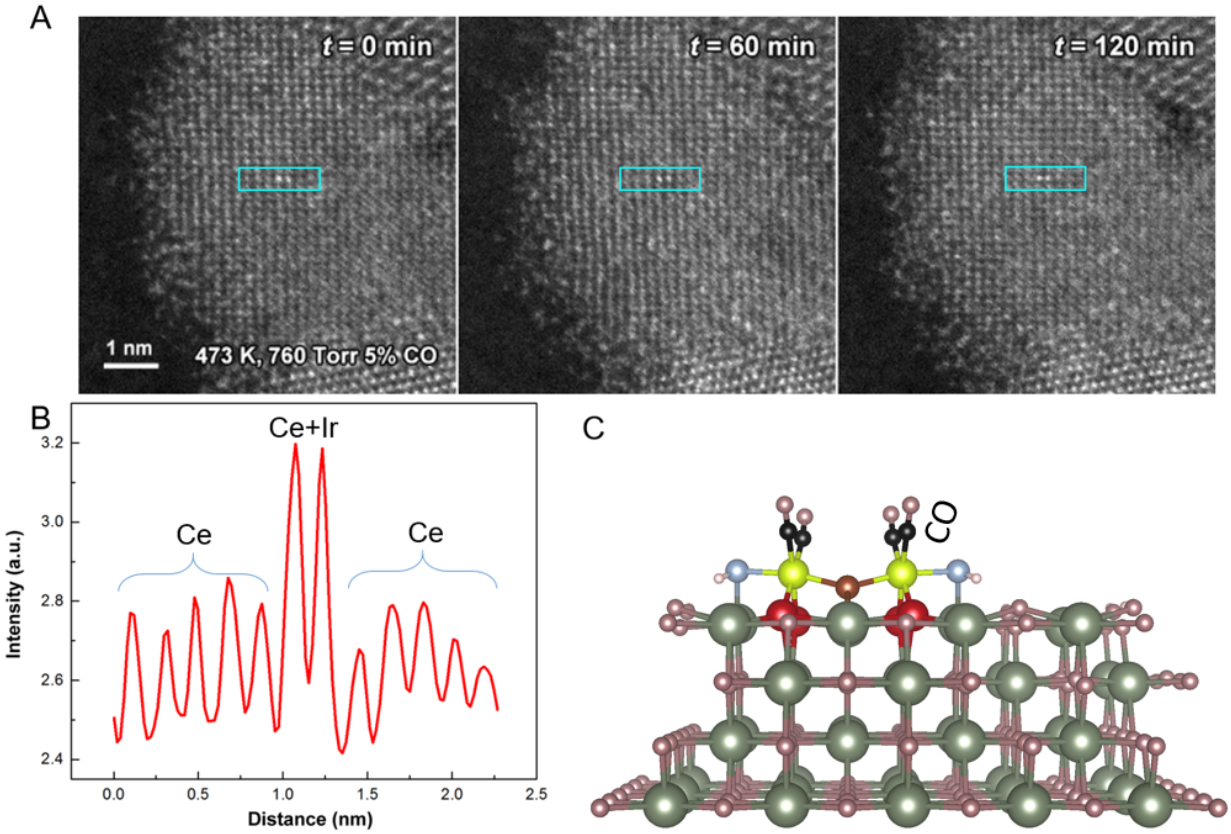

Figure S9. *In situ* HAADF-STEM images showing the mobility of DHC (**A**) at pure CO gas phase (760 Torr of 5% CO, 473 K) to mimic the CO-related reaction condition, such as CO oxidation. (**B**) Normalized intensity profile. (**C**) DFT-optimized DHC model under CO condition.

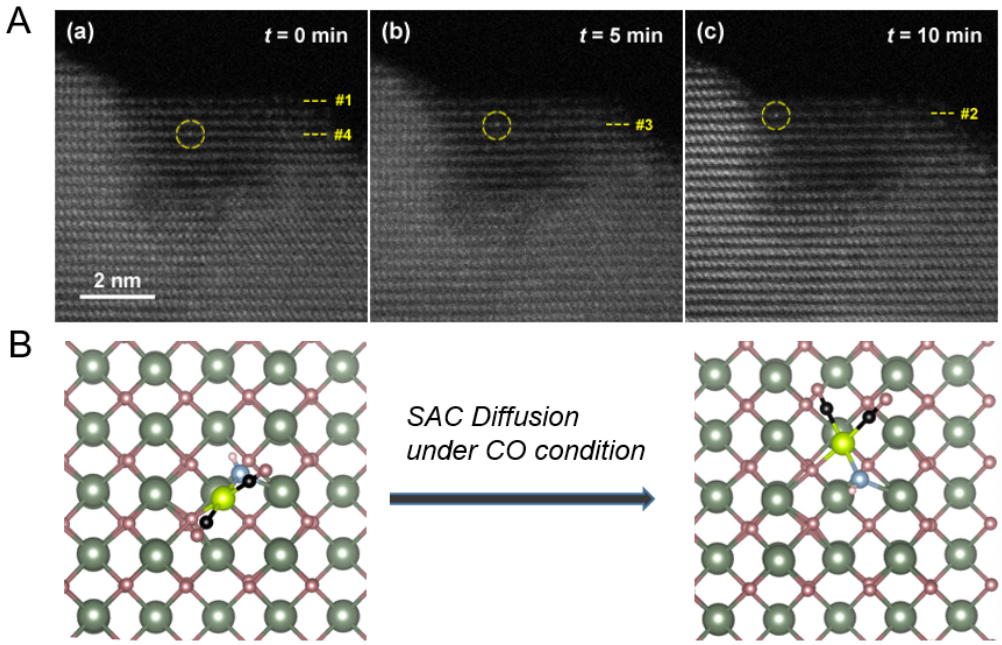

Figure S10. (**A**) *In situ* HAADF-STEM images showing the mobility of SAC at the pure CO gas phase (760 Torr of 5% CO, 473 K). The number is used to mark the crystal facets from the top. (**B**) DFT-optimized SAC before and after the diffusion.

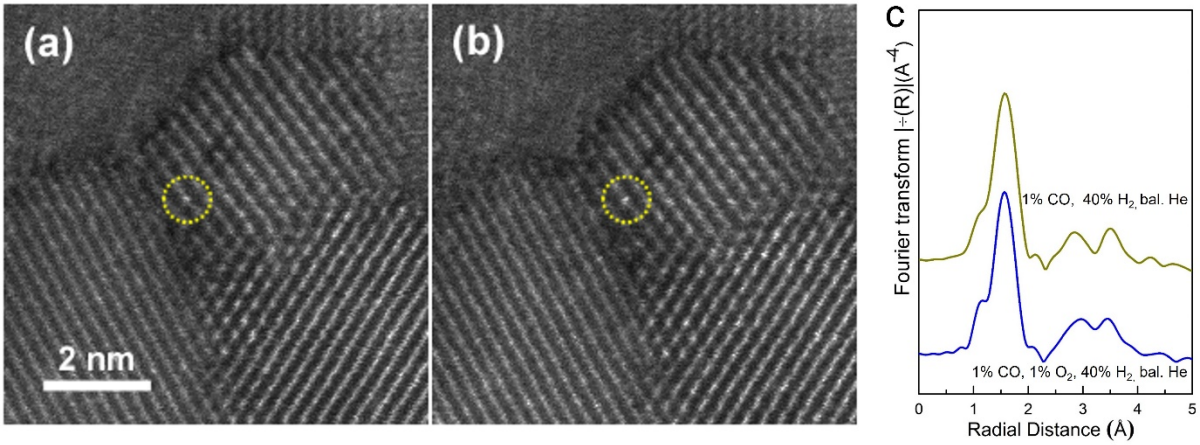

Figure S11. (**A** and **B**) *In situ* STEM result showing negligible electron beam effect of image acquisition on the Ir species. Two *in-situ* HAADF-STEM images of Ir SAC/CeO_2 under 760 Torr of N_2 at 473 K at different time periods. Yellow circles highlight the Ir single atoms. (**C**) Ex-situ EXAFS spectra of Ir DHCs after 12h CO+H_2 and Ir DHC under 12h CO+H_2, then switch to CO+H_2+O_2), showing that the absence of O_2 in operando STEM study might not trigger significant structure change for Ir DHC.

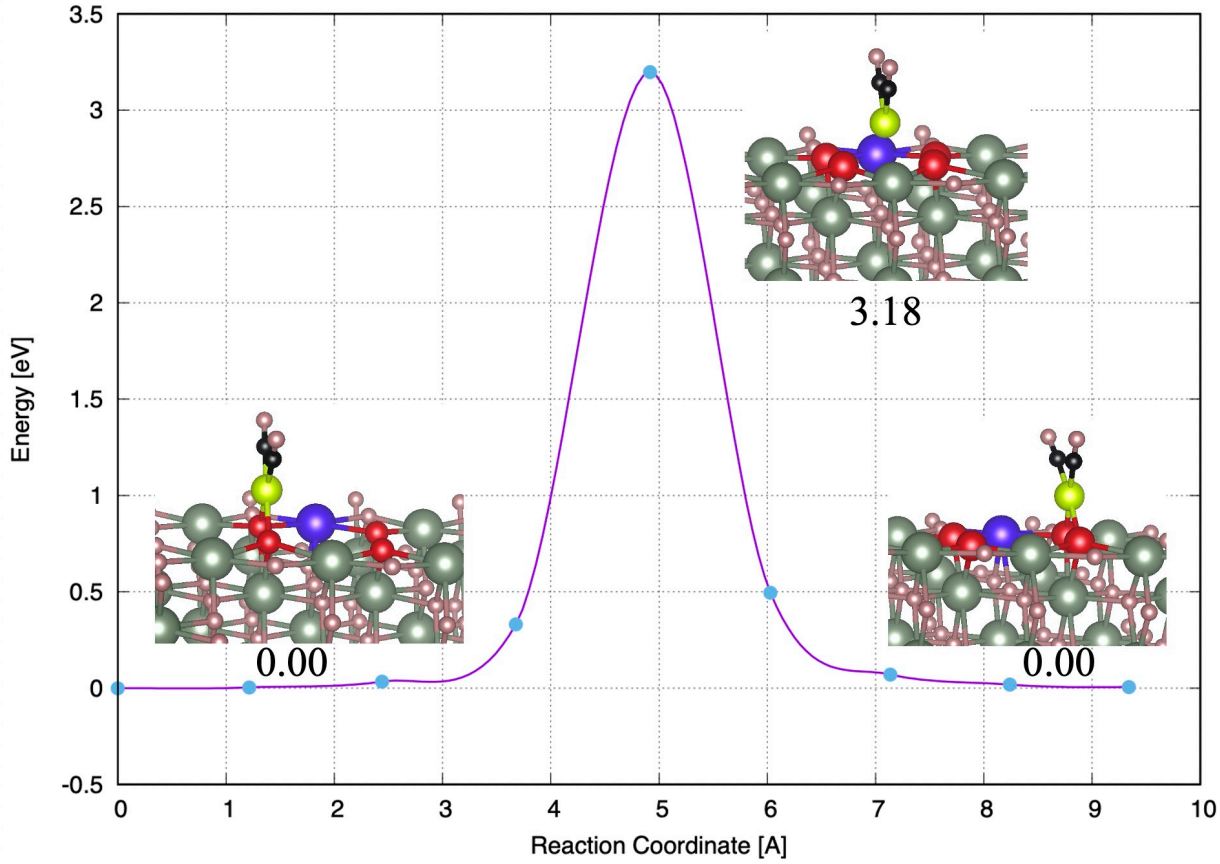

Figure S12. Minimum-energy pathway (MEP) of Ir SAC diffusion assisted by two CO on an unreduced CeO_2 surface. We considered Ir atom diffusion on an unreduced CeO_2 (110) surface assisted by two CO molecules. When an Ir atom is adsorbed on CeO_2 surface, it transfers an electron to reduce a nearby surface Ce(IV) (shown in the blue sphere). Although CO has been suggested to promote atom diffusion on several metal-oxide supports, the diffusion of Ir atom on an unreduced CeO_2 surface has a large barrier of 3.2 eV according to our calculations.

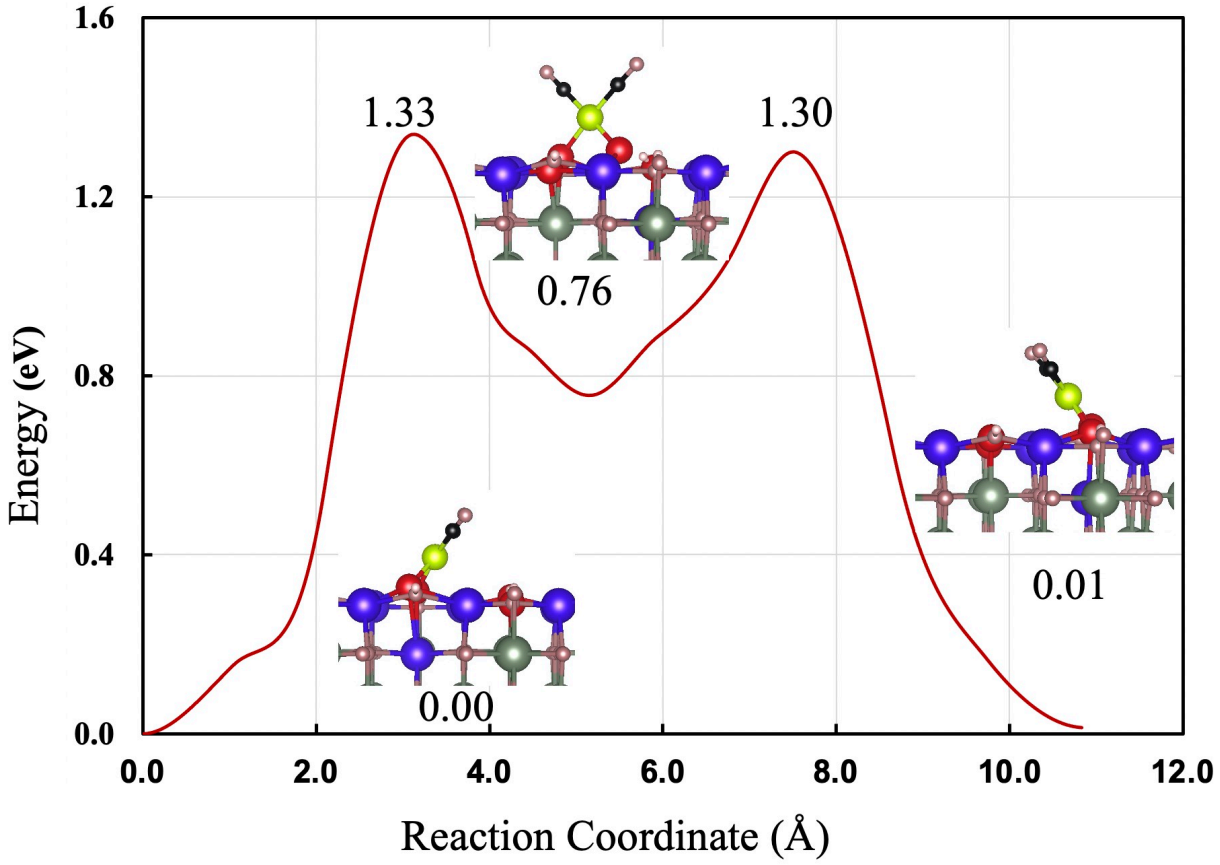

Figure S13. Minimum-energy pathway (MEP) of Ir SAC diffusion assisted by two CO on a reduced CeO_2 surface with a sublayer Ce(III) center. By preparing a highly reduced CeO_2 surface with a sublayer Ce(III) center, the diffusion of Ir SAC on a reduced CeO_2 surface is feasible with an energy barrier ~ 1.3 eV. The diffusion of Ir SAC under a reducing environment can account for its unsatisfied stability compared to Ir DHC.

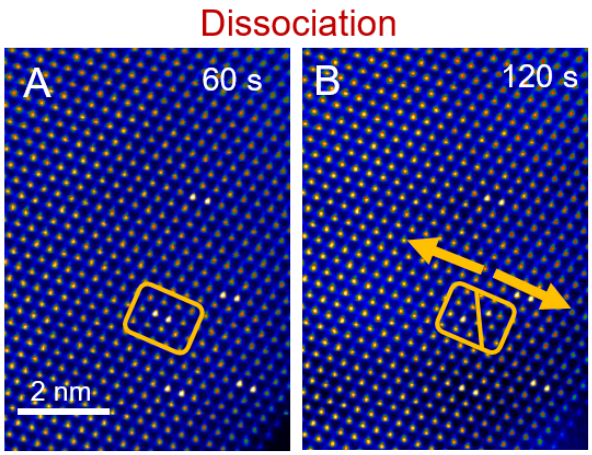

Figure S14. (A) Evolution of Ir DHC during intentional strong electron beam irradiation in the vacuum chamber for the following times: 60 s (**A**), 120 s (**B**).

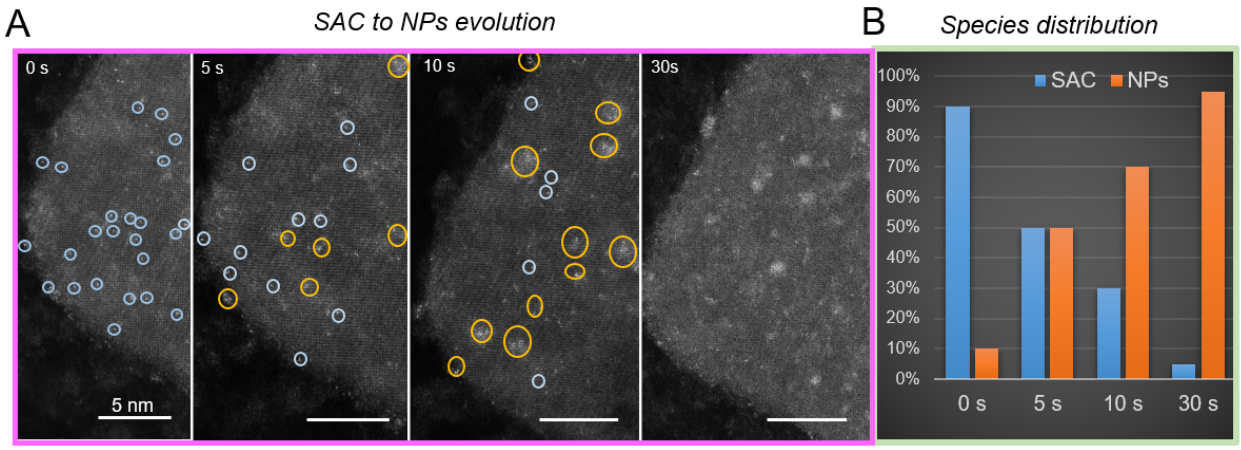

Figure S15. (A) Evolution of Ir SAC during the intentional strong electron beam irradiation in the vacuum chamber for the following times: 0 s, 5 s, 10 s, and 30 s. The circles are drawn around SAC (blue) and cluster (orange). The size distribution (**B**) is based on species counted in (**A**).

More discussions of the catalytic cycle in Figure 4C

The oxidation of CO by interfacial O in intermediate **I** forms intermediate **II** with a chemically-adsorbed CO_2 (Figure S20). Subsequent CO_2 release yields a square planar Ir structure (intermediate **III**). It is noted that our DFT predicted structure is similar to Vaska's complex (Figure S22 and Table S3)[26] with known activity to activate O_2 for CO oxidation [27]. The geometry and electronic configuration of intermediate **III**, as well as its similarity to the Vaska's complex, led us to assign oxidation state +1 for the Ir centers. The O–O bond length in intermediate **IV** is 1.46 Å (Table S4), which corresponds to a peroxide, suggesting two electrons are transferred from the Ir center to O_2 form O_2^{2-} (active interfacial O species)[28a]. The electron transfer between the Ir center and O_2 is further confirmed by Bader charge analysis on the Ir center and O_2 ligand (Table S6). The activation of O_2 by intermediate **III** can be classified as an oxidative addition which is a well-studied reaction for Ir(I) complexes in organometallics. The formation of intermediate **III** by activated interfacial O atom and adsorbed CO molecules is a reductive elimination which is common for a 6-coordinated Ir(III) complex. The overall reaction energy change is -6.5 eV corresponds to the reaction $2CO + O_2 \rightarrow 2CO_2$, which is consistent with the previous report on calculations for the catalytic CO oxidation[23].

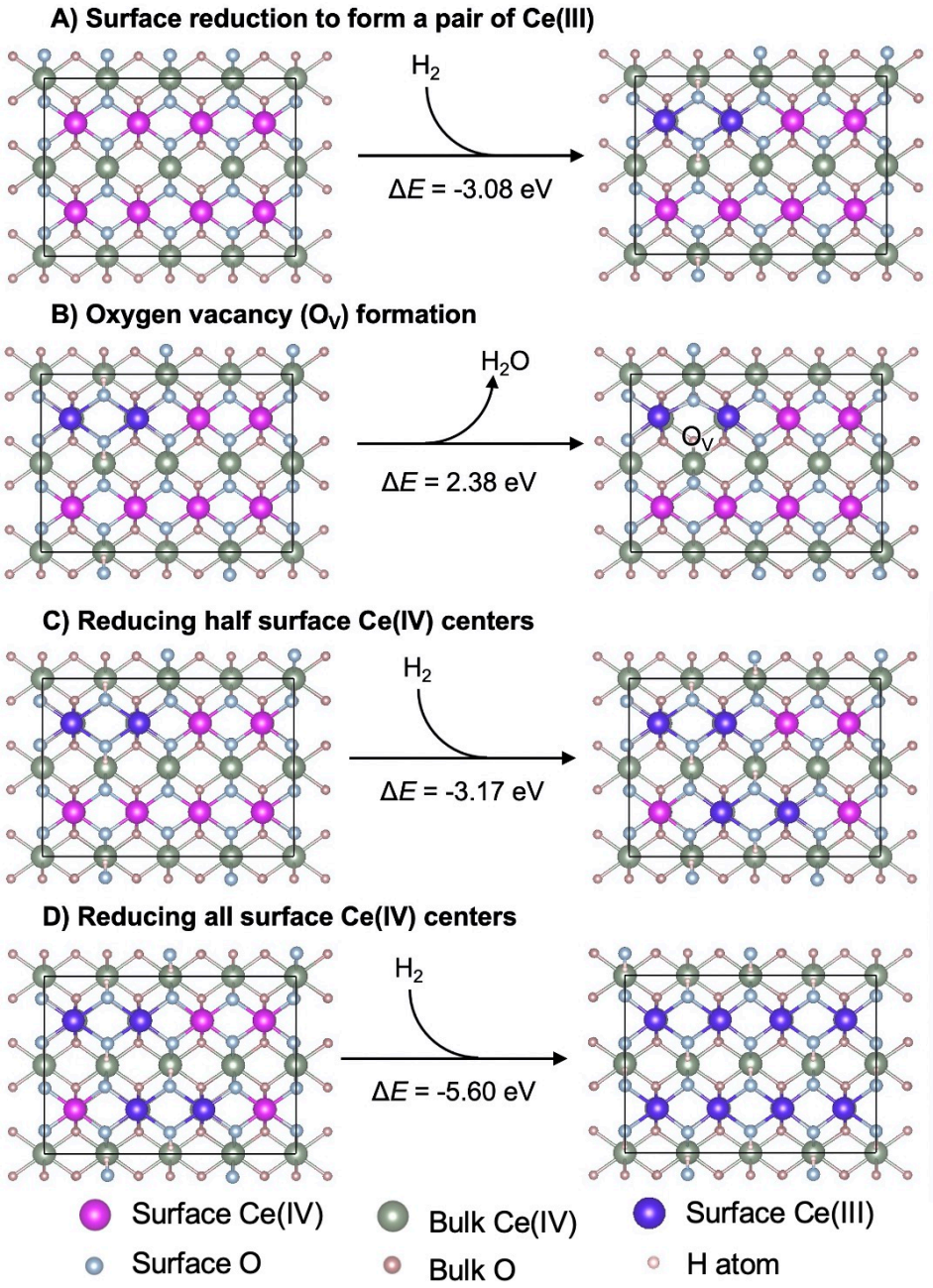

Figure S16. Surface reduction of CeO_2 (110) in H_2 atmosphere (top view). The reduction of the CeO_2 (110) surface by H_2 is highly exothermic, even when all the surface Ce(IV) centers have been reduced to Ce(III). The reduced Ce(III) center has an electronic configuration of $[Xe]4f^1$ and its atomic magnetic moment is ~0.96 μ_B according to our calculation. (A) The reaction energy of surface reduction is about ~ -3 eV/H_2. Surface hydroxyl groups are formed during the surface reduction process. (B) The generation of oxygen vacancy on reduced CeO_2 surface is highly endothermic (ΔE = 2.38 eV). (C) The energy for reducing half surface Ce centers is 3.17 eV; (D) the energy for reducing all surface Ce cetners is even greater, 5.60 eV. Therefore, under reaction conditions with the presence of H_2, the CeO_2 (110) surface is most likely to be reduced with a large number of surface hydroxyl groups as suggested by previous experimental studies [29].

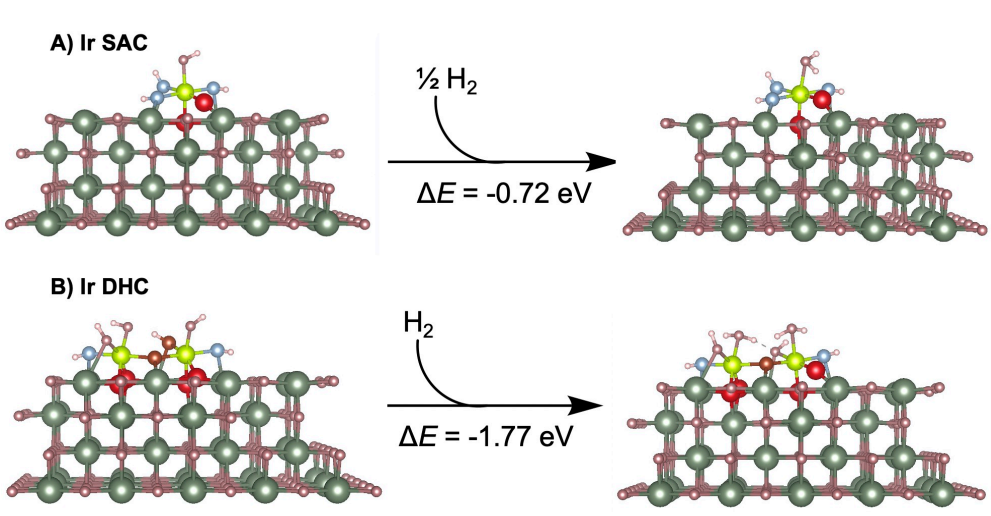

Figure S17. Reduction of Ir SAC and DHC with H_2. The reduction of the Ir(IV) centers in (A) Ir SAC and (B) DHC by H_2 is thermodynamically very favorable, with a reaction energy change of -1.44 eV / H_2 and -1.77 eV, respectively. Upon the reduction, the open-shell Ir(IV) centers, with the d^5 electronic configuration and atomic magnetic moments of 0.67 μ_B (Bohr magneton), become closed-shell Ir(III) centers with d^6 electronic configuration and zero magnetic moments at Ir centers. Therefore, the Ir centers in Ir SAC and DHC are most likely to be in the oxidation state (III). Further reducing Ir does not produce Ir centers in oxidation state II. Instead, surface Ce(IV) centers get reduced to Ce(III), as indicated by negative reaction energies of surface reduction (Figure S16). Thus, it is reasonable to assume that Ir(III) centers are in the oxidation state (III) under reaction conditions while surface Ce(IV) has been reduced to Ce(III).

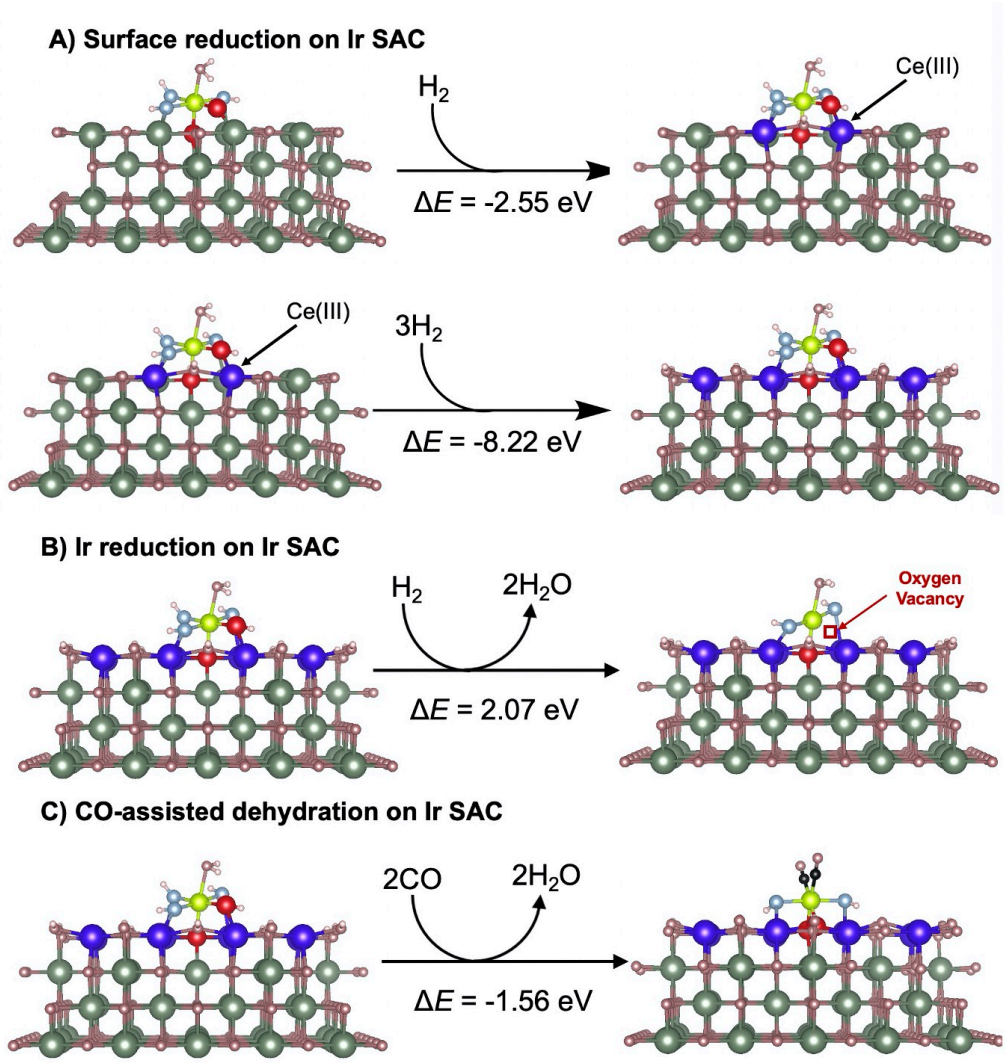

Figure S18. Reduction of Ir SAC using H_2. (A) The energy of reducing Ir SAC by H_2 without (top panel) and with (bottom panel) the participation of Ce. (B) The energy of reducing Ir SAC that involves the formation of oxygen vacancies. (C) The energy of dehydration on Ir SAC assisted by CO. Reduction of the open-shell Ir(IV) center to Ir(III) using H_2 on the CeO_2 (110) surface is thermodynamically favorable (Figure S17). However, the further reduction will not reduce Ir(III) to Ir(I), but reduce nearby Ce(IV) centers to Ce(III) with a change of reaction energy of -2.6 eV (Figure S19A). Further reduction of surface Ce(IV) centers has similar reaction energy changes (~ -2.7 eV per H_2), slightly less negative than those on the bare CeO_2 (110) surface. Based on the changes in reaction energy, one would expect that the Ir SAC under H_2 atmosphere, the reaction condition performed for the PROX reaction, is likely to have Ir(III) centers on reduced CeO_2 surfaces. Even after all the surface Ce(IV) centers have been reduced, the further reduction of an Ir(III) center to Ir(I) and generating an oxygen vacancy is still energetically unfavorable (Figure S18B). Nevertheless, this reaction can be shifted toward the right at an elevated temperature since it is an entropy-increasing reaction. Due to the strong interaction between Ir and CO, the CO can assist the dehydration of Ir SAC to form di-carbonyl Ir(III) complex (Figure S18C). We anticipate the same process occurs for Ir DHC under the PROX condition, where di-carbonyl Ir(III) dimers connected by a mono-μ-oxo bridge are formed on the reduced CeO_2 surface, as indicated by *in situ* DRIFTS spectra. In the following modeling of catalytic mechanisms of Ir SAC and DHC, we always use the reduced surface model (surface Ce in oxidation state +3).

Since Ce(III) has an electronic configuration of [Xe]$4f^1$ and unpaired f electrons which usually cause SCF convergence problems, we model the eight surface Ce(III) centers ferromagnetically coupled with each other to have better SCF convergence.

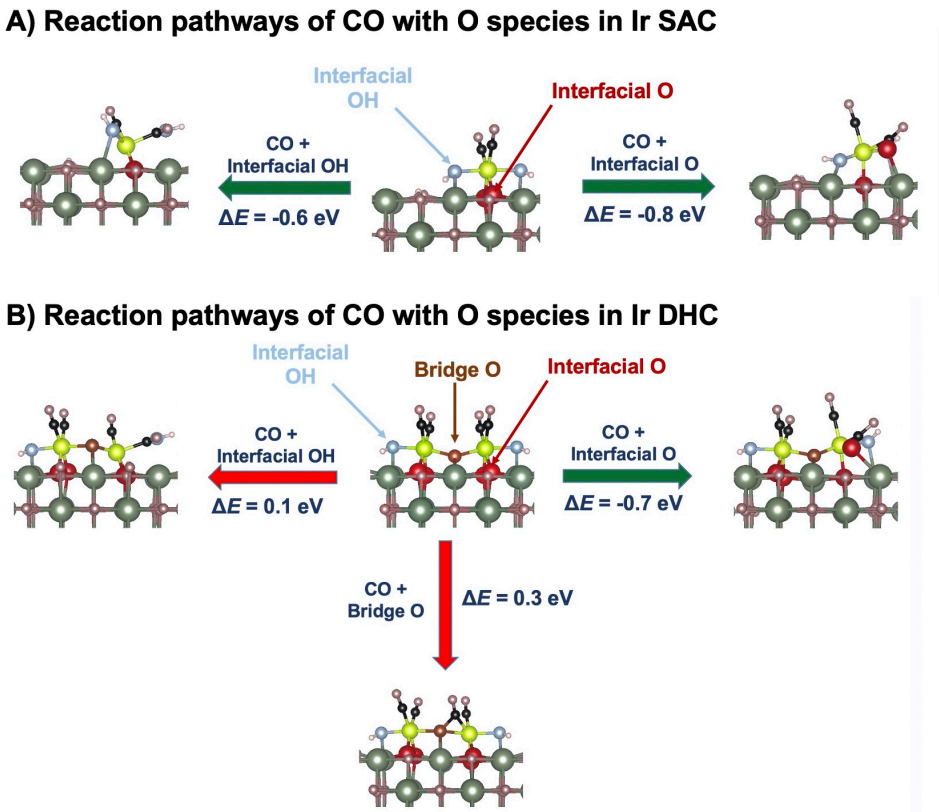

Figure S19. Reaction pathways of CO with different O species in A) Ir SAC and B) Ir DHC. There are only interfacial O species in Ir SAC to anchor it on the CeO_2 surface. The reaction of CO with both interfacial O and interfacial OH are both energetically favorable due to the flexibility of single Ir on the CeO_2 surface. Therefore, Ir SAC should be catalytic active for both CO oxidation and reverse water gas shift reaction in which CO couples with interfacial OH. In the contrast, Ir DHC is more rigid than Ir SAC with both Ir centers held together by a mono-μ-oxo bridge. The reaction of CO with interfacial OH and bridge O is energetically unfavorable, while the reaction of CO with interfacial O is energetically in Ir DHC as favorable as that in Ir SAC. The unique bridge O in Ir DHC affords its extreme stability.

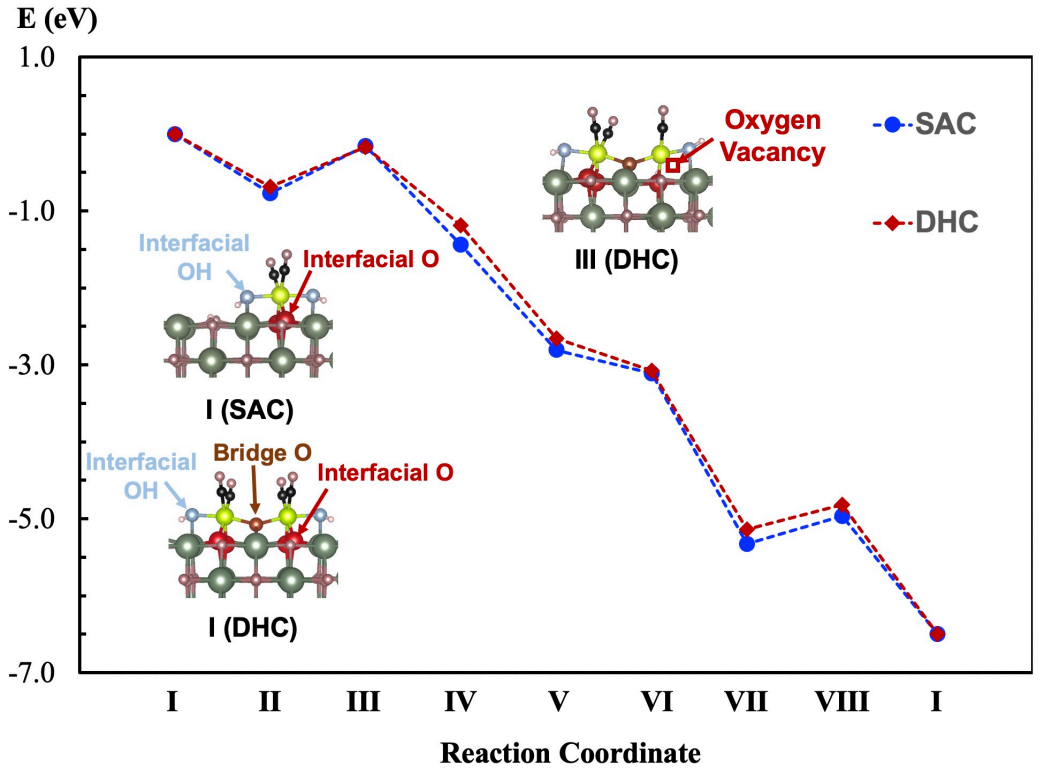

Figure S20. Energy profiles along the reaction path of CO oxidation catalyzed by Ir SAC and DHC. The relative energies of intermediates of CO oxidation catalyzed by Ir SAC and DHC are similar. Ir DHC can be regarded as two Ir SACs forming a mono-μ-oxo bridge to connect together. During catalysis, only one Ir is active, while the other serves as an anchor to prevent Ir atom diffusion and other side reactions.

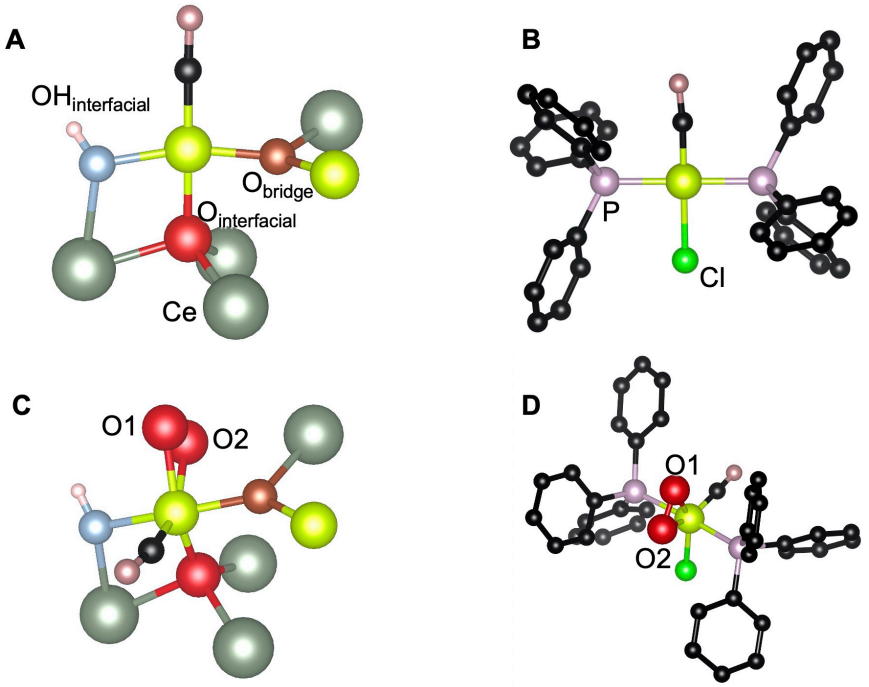

Figure S21. Comparison of intermediate III (A) and IV (C) with the Vaska's complex (B) and dioxygen-Vaska's complex (D). The Vaska's complex (**B**) (*trans*-carbonylchlorobis-(triphenylphosphine)iridium(I)) is a well-studied Ir complex with d^8 electronic configuration and square planar geometry [30, 31]. It can absorb O_2 to form dioxygen-Vaska's complex (**D**) which has a d^6 Ir(III) center and trigonal bipyramidal geometry [32, 33]. The intermediate **III** (**A**) in our proposed catalytic cycle resembles the structure of the Vaska's complex, where one interfacial OH and a bridge O atom resemble the two P atoms in the triphenylphosphine ligands and one interfacial O atom resembles the chloride ligand. The O_2 adding complex (intermediate **IV**, **C**) in our proposed catalytic cycle resembles the dioxygen-Vaska's complex (**D**) which has been demonstrated to be able to oxidize CO to form a C–O bond [34]. The structural similarity between our Ir DHC and the Vaska complex implicates that the bridge O may serve as an anchoring group to stabilize the Ir center on the center rather than directly involved in the catalytic CO oxidation, which is consistent with our DFT suggested reaction pathway and *in situ* STEM results. The comparison between intermediates **III** and **IV** with (dioxygen-)Vaska's complexes helps to assign the formal oxidation state of Ir in **III** and **IV**.

Table S1. Calculated surface formation energy of CeO_2 (110) surface with various Ce–O layers

	$E_{surface}$ (J/m^2)
4 layers	1.03
5 layers	1.04
6 layers	1.03

Table S2. Fitting and structural parameters in the EXAFS simulation of Ir DHC models with mono-μ-oxo bridge and bi-μ-oxo bridge model.

mono-μ-oxo bridge Ir dimer			
Fitting Parameters			
ΔE_0	3.35 eV		
S_0^2	0.95		
k range	3.0 – 12.0 Å^{-1}		
R range	1.0 – 4.0 Å		
Structural Parameters			
Scattering path	CN[a]	*R* (Å)[b]	σ^2 (Å^2)
Ir–O	6	Ir1: 1.97, 1.98, 2.03, 2.03, 2.04, 2.08 (2.02) Ir2: 1.95, 2.02, 2.02, 2.04, 2.06, 2.10 (2.03)	0.002
Ir–Ir	1	3.67	0.002
Ir–Ce	5	Ir1: 3.47, 3.58, 3.60, 3.76, 3.86 (3.65) Ir2: 3.47, 3.52, 3.70, 3.74, 4.06 (3.70)	0.002
bi-μ-oxo bridge Ir dimer			
Fitting Parameters			
ΔE_0	3.35 eV		
S_0^2	1.00		
k range	3.0 – 12.0 Å^{-1}		
R range	1.0 – 4.0 Å		
Structural Parameters			
Scattering path	CN[a]	*R* (Å)[b]	σ^2 (Å^2)
Ir–O	6	Ir1: 1.94, 1.99, 2.04, 2.04, 2.08, 2.11 (2.03)	0.001
Ir–Ir	1	3.18	0.002
Ir–Ce	5	Ir1: 3.42, 3.62, 3.76,3.83, 4.13 (3.75)	0.012

[a] CN denotes Coordination Number. Coordination numbers in our simulation are determined from our DFT optimized structure rather than treated as fitting parameters.
[b] The distances from our optimized structure are used in the ab initio real Green function calculations in the FEFF program. The DFT optimized bond lengths are given in the unit of Å. The numbers in the parentheses are average bond lengths. We also considered treating the Ir–O bond distances adjustable parameters described by deviations (Δr) from DFT optimized bond distances. The fitting to experimental EXAFS gives $\Delta r = -0.0012$ Å, demonstrating the reliability of bond distances from our DFT calculations.

Table S3. Comparison of geometric parameters of intermediate III and the Vaska's complex

Intermediate **III**		Vaska's complex[a]	
r(Ir–C) / Å	1.80	r(Ir–C) / Å	1.79
r(Ir–O_i)[b] / Å	2.07	r(Ir–Cl) / Å	2.38
r(Ir–OH_i)[b] / Å	2.07	r(Ir–P) / Å	2.33
r(Ir–O_b)[b] / Å	2.02	r(Ir–P) / Å	2.33
θ(O_i–Ir–C) / °	179	θ(Cl–Ir–C) / °	180
θ(OH_i–Ir–O_b) / °	166	θ(P–Ir–P) / °	180
θ(Ir–C–O) / °	178	θ(Ir–C–O) / °	175
φ(OH_i–Ir–C–O_b) / °	174	φ(P–Ir–C–P) / °	180
φ(O_i–Ir–O_b–C) / °	179	φ(Cl–Ir–P–C) / °	180

[a] The X-ray crystal structure is taken from Ref. *31*.
[b] O_i, OH_i, and O_b denote interfacial O, interfacial OH, and bridge O atoms, respectively. We should not compare the exact numbers of Ir–O bond lengths with Ir–Cl and Ir–P bond lengths. We list them here to show their corresponding relation with ligands in the Vaska's complex.

Table S4. Comparison of geometric parameters of intermediate IV and the dioxygen-Vaska's complex

Intermediate **IV**		dioxygen-Vaska's complex[a]	
r(Ir–C) / Å	1.82	r(Ir–C) / Å	1.79
r(Ir–O1)[b] / Å	2.02	r(Ir–O1)[b] / Å	2.05
r(Ir–O2)[b] / Å	2.06	r(Ir–O2)[b] / Å	2.05
r(O1–O2)[b] / Å	1.46	r(O1–O2)[b] / Å	1.47
θ(O_i–Ir–C) / °	105	θ(Cl–Ir–C) / °	96
θ(O_i–Ir–O2) / °	102	θ(Cl–Ir–O2) / °	108
θ(O1–Ir–C) / °	111	θ(O1–Ir–C) / °	114
θ(O1–C–O2) / °	42	θ(O1–C–O2) / °	42
θ(Ir–C–O) / °	171	θ(Ir–C–O) / °	176
φ(C–Ir–O1–O2) / °	175	φ(C–Ir–O1–O2) / °	176
φ(O_s–Ir–O2–O1) / °	178	φ(Cl–Ir–O2–O1) / °	175

[a] The X-ray crystal structure is taken from Ref. *33*. The disorder of the chloride and CO ligands results in two configurations. The reported bond lengths, bond angles, and dihedral angles are the average of the two configurations.
[b] The labels of O1 and O2 are shown in Figure S21.
[c] The bond length of O1–O2 in intermediate **IV** and the dioxygen-Vaska's complex falls into the region of peroxide [35], indicating that two electrons from the Ir(I) center are transferred to the adsorbed O_2 molecule, forming an activated O_2^{2-} species which is ready for the following CO oxidation.

Table S5. The oxidation numbers, numbers of d electrons, coordination numbers and geometries of all intermediates in the proposed catalytic cycle involving the Ce(I) center shown in Figure 4C.

Intermediate	Oxidation Number	Number of d electrons	Coordination Number	Geometry
I	+3	6	6	Octahedral
II	+3	6	5	Square pyramidal
III	+1	8	4	Square planar
IV	+3	6	5(6)	Trigonal bipyramidal
V	+4	5	6	Octahedral
VI	+4	5	6	Octahedral
VII	+3	6	5	Square pyramidal
VIII	+3	6	5	Square pyramidal

The oxidation of the first CO molecule in intermediate **I** results in the 5-coordinated Ir(III) center (intermediate **II**) in a square pyramidal geometry, which subsequently releases a CO_2 molecule to form intermediate **III** with a square planar Ir(I) center. The oxidation of the first CO molecule (intermediate **I** → intermediate **III**) is a reductive elimination [36] to form a C–O bond between an interfacial O atom and adsorbed CO molecule. The oxidation state of the Ir center decreases from +3 to +1 from intermediate **I** to **III**, as reflected by the decrease of partial charge on the Ir center according to the Bader charge analysis (Table S6). However, in intermediate **II**, there is still significant d electron transfer from the Ir center to CO_2. The binding of O_2 to intermediate **III** involves the transfer of two electrons from the Ir(I) center to O_2 to form O_2^{2-} in intermediate **IV**, which is confirmed by the Bader charge analysis (Table S6), as well as the O–O bond length (Table S7). Intermediate **IV** further undergoes O–O bond cleavage to form intermediate **V** with both the Ir(III) can a nearby Ce(III) being oxidized.

Table S6. Bader charges of the Ir center and ligands in intermediates in the proposed catalytic cycle.

	Ir	Ce	CO (spectator)	O_2	CO (substrate)	CO_2 (product)
I	1.74	2.10	-0.18		-0.20	
II	1.23	2.10	-0.32			-0.75
III	0.90	2.06	-0.51			
IV	1.62	2.15	-0.38	-1.11		
V	1.86	2.39	-0.23	-2.07		
VI	1.87	2.39	-0.24	-2.06	0.02	
VII	1.55	2.12	-0.31			-0.01
VIII	1.56	2.10	-0.31			

The partial charges from the Bader charge analysis enable us to study charge distribution among atoms and groups in a molecule. A neutral atom or molecule has zero charge. One would expect that an atom with a positive oxidation number would have a positive Bader charge, while an atom with a negative oxidation number would have a negative Bader charge. Indeed, the Bader charge of the Ir center in all intermediates in our proposed catalytic cycle are all positive, and the charge increases when the oxidation number of Ir increases. The spectator CO ligand has a negative Bader charge in all intermediates due to the d-π* back donation. The adsorbed O_2 species has Bader charges of -1.11 in intermediate **IV**, corresponding to O_2^{2-}. The sum of partial charges on the two O atoms becomes -2.07 after the O–O bond cleavage in intermediate **IV**, corresponding to $2O^{2-}$. The CO substrate in intermediate **VI** has a Bader charge of 0.02, indicating it is essentially a neutral ligand as in the isolated CO molecule, consistent with the physical adsorption of CO in intermediate **VI**. In contrast, the CO substrate in intermediate **I** has a Bader charge of -0.20, indicating it gets electron density from Ir, consistent with the d-π* back donation in the chemically adsorbed CO in intermediate **I**. Similarly, the first and second CO_2 products are chemically and physically adsorbed at the Ir center in intermediates **II** and **VII**, as suggested by their Bader charges (Table S6) and bond lengths (Table S7).

Table S7. Optimized key bond lengths in intermediates in the proposed catalytic cycle.

	CO (spectator)	O_2	CO (substrate)	CO_2 (product)	
	r(C–O) / Å	*r*(O–O) / Å	*r*(C–O) / Å	*r*(C–O1) / Å	*r*(C–O2) / Å
I	1.16		1.16		
II	1.17			1.23	1.28
III	1.18				
IV	1.17	1.46			
V	1.17	2.53			
VI	1.17	2.53	1.14		
VII	1.17			1.17	1.18
VIII	1.17				

References for Supplementary Materials:

1. J. M. Thomsen, S. W. Sheehan, S. M. Hashmi, J. Campos, U. Hintermair, R. H. Crabtree, G. W. Brudvig, *J. Am. Chem. Soc.* **136**, 13826-13834 (2014).
2. U. Hintermair, S. M. Hashmi, M. Elimelech, R. H. Crabtree, *J. Am. Chem. Soc.* **134**, 9785-9795 (2012).
3. G. Kresse, J. Hafner, *Phys. Rev. B* **47**, 558-561 (1993).
4. G. Kresse, J. Hafner, *Phys. Rev. B* **49**, 14251-14269 (1994).
5. G. Kresse, J. Furthmüller, *Comput. Mater. Sci.* **6**, 15-50 (1996).
6. G. Kresse, J. Furthmüller, *Phys. Rev. B* **54**, 11169-11186 (1996).
7. J. P. Perdew, K. Burke, M. Ernzerhof, *Phys. Rev. Lett.* **77**, 3865-3868 (1996).
8. P. E. Blöchl, *Phys. Rev. B* **50**, 17953-17979 (1994).
9. G. Kresse, D. Joubert, *Phys. Rev. B* **59**, 1758-1775 (1999).
10. S. Grimme, S. Ehrlich, L. Goerigk, *J. Comput. Chem.* **32**, 1456-1465 (2011).
11. S. L. Dudarev, G. A. Botton, S. Y. Savrasov, C. J. Humphreys, A. P. Sutton, *Phys. Rev. B* **57**, 1505-1509 (1998).
12. D. O. Scanlon, N. M. Galea, B. J. Morgan, G. W. Watson, *J. Phys. Chem. C* **113**, 11095-11103 (2009).
13. M. Nolan, *J. Chem. Phys.* **136**, 134703 (2012).
14. Y. Zhao, K. R. Yang, Z. Wang, X. Yan, S. Cao, Y. Ye, Q. Dong, X. Zhang, J. E. Thorne, L. Jin, K. L. Materna, A. Trimpalis, H. Bai, S. C. Fakra, X. Zhong, P. Wang, X. Pan, J. Guo, M. Flytzani-Stephanopoulos, G. W. Brudvig, V. S. Batista, D. Wang, *Proc. Nat. Acad. Sci.* **115**, 2902-2907 (2018).
15. H. J. Monkhorst, J. D. Pack, *Phys. Rev. B* **13**, 5188-5192 (1976).
16. C. Artini, M. Pani, M. M. Carnasciali, M. T. Buscaglia, J. R. Plaisier, G. A. Costa, *Inorg. Chem.* **54**, 4126-4137 (2015).
17. G. Henkelman, B.P. Uberuaga, and H. Jónsson, *J. Chem. Phys*. **113**, 9901 (2000).
18. A. Heyden, A. T. Bell, F. J. Keil, *J. Chem. Phys.* **123**, 224101 (2005).
19. J. J. Rehr, R. C. Albers, *Rev. Mod. Phys.* **72**, 621−654 (2000).

20. M. Newville, *J. Synchrotron Radiat.* **8**, 322−324 (2001).
21. J. Lin, B. Qiao, J. Liu, Y. Huang, A. Wang, L. Li, W. Zhang, L. F. Allard, X. Wang, T. Zhang, *Angew. Chem. Int. Ed.* **51**, 2920-2924 (2012).
22. Y. Huang, A. Wang, X. Wang, T. Zhang, *Int. J. Hydrog. Energy* **32**, 3880-3886 (2007).
23. B. Qiao, A. Wang, X. Yang, L. F. Allard, Z. Jiang, Y. Cui, J. Liu, J. Li, T. Zhang, *Nat. Chem.* **3**, 634-641 (2011).
24. G. Chen, Y. Zhao, G. Fu, P. N. Duchesne, L. Gu, Y. Zheng, X. Weng, M. Chen, P. Zhang, C.-W. Pao, J.-F. Lee, N. Zheng, *Science* **344**, 495-499 (2014).
25. Q. Fu, W.-X. Li, Y. Yao, H. Liu, H.-Y. Su, D. Ma, X.-K. Gu, L. Chen, Z. Wang, H. Zhang, B. Wang, X. Bao, *Science* **328**, 1141-1144 (2010).
26. L. Vaska, J. W. DiLuzio, *J. Am. Chem. Soc.* **83**, 2784-2785 (1961).
27. H. J. Lawson, J. D. Atwood, *J. Am. Chem. Soc.* **110**, 3680-3682 (1988).
28. J. Cramer, W. B. Tolman, K. H. Theopold, A. L. Rheingold, *Proc. Natl. Acad. Sci. U.S.A.* **100**, 3635-3640 (2003).
29. D. Schweke, L. Shelly, R. Ben David, A. Danon, N. Kostirya, and S. Hayun, *J. Phys. Chem. C* **124**, 6180-6187 (2020).
30. L. Vaska, J. W. DiLuzio, *J. Am. Chem. Soc.* **83**, 2784-2785 (1961).
31. M. Rowen Churchill, J. C. Fettinger, L. A. Buttrey, M. D. Barkan, J. S. Thompson, *J. Organomet. Chem.* **340**, 257-266 (1988).
32. L. Vaska, *Acc. Chem. Res.* **1**, 335-344 (1968).
33. H. Lebel, C. Ladjel, F. Bélanger-Gariépy, F. Schaper, *J. Organomet. Chem.* **693**, 2645-2648 (2008).
34. H. J. Lawson, J. D. Atwood, *J. Am. Chem. Soc.* **110**, 3680-3682 (1988).
35. C. J. Cramer, W. B. Tolman, K. H. Theopold, A. L. Rheingold, *Proc. Natl. Acad. Sci. U.S.A.* **100**, 3635 (2003).
36. R. H. Crabtree, *The Organometallic Chemistry of the Transition Metals*. (John Wiley & Sons, Inc., Hoboken, New Jersey, 2005).